

Nanostructured lead-free ferroelectric  $\text{Na}_{0.5}\text{Bi}_{0.5}\text{TiO}_3\text{--BaTiO}_3$  whiskers: synthesis mechanism and structureDeepam Maurya,<sup>\*a</sup> Valeri Petkov,<sup>b</sup> Ashok Kumar<sup>c</sup> and Shashank Priya<sup>a</sup>

Received 7th January 2012, Accepted 3rd February 2012

DOI: 10.1039/c2dt00045h

Nanostructured lead-free ferroelectric  $\text{Na}_{0.5}\text{Bi}_{0.5}\text{TiO}_3\text{--BaTiO}_3$  (NBTBT) whiskers with a high aspect ratio were synthesized topochemically using  $\text{Na}_2\text{Ti}_6\text{O}_{13}$  (NTO) as a host structure for the first time. High energy X-ray diffraction coupled with an atomic pair distribution function (PDF) and Raman scattering analyses were used to confirm the average structure of the lead-free NBTBT whiskers, which was found to be rhombohedral, *i.e.* a ferroelectric enabling type. High resolution transmission electron microscopic (HRTEM) analysis revealed local monoclinic-type structural distortions, indicating a modulated structure at the nanoscale in the morphotropic phase boundary (MPB) composition of the lead-free NBTBT whiskers. The structural rearrangement during the synthesis of the lead-free NBTBT whiskers was found to occur *via* translation of the edge shared octahedra of NTO into a corner sharing coordination. High temperature morphological changes that depict the disintegration of the isolated whiskers into their individual grains due to the higher grain boundary energy have been found to occur in close analogy with Rayleigh-type instability.

## Introduction

Ferroelectric perovskite oxides in the form of single crystals, polycrystalline ceramics and thin or thick films constitute an important class of materials widely used in capacitors, electro-mechanical systems, ferroelectric memories, *etc.*<sup>1,2</sup> Moreover, in recent years, owing to the shrinking size of electrical and electro-mechanical components, fabrication and characterization of micro- and nano-sized perovskite oxides have attracted much attention.<sup>3–8</sup> Ferroelectric nanostructures with high aspect ratios are highly desired but their synthesis is extremely challenging since, at reduced dimensions, most perovskites adopt a structure with cubic symmetry resulting in a highly isotropic shape during high temperature processing. There have been several approaches to obtain nano-structured materials with anisotropic shapes, such as the template-directed method,<sup>9</sup> vapor phase synthesis,<sup>10</sup> vapor–liquid–solid (VLS) growth,<sup>11</sup> the solution–liquid–solid (SLS) technique,<sup>12</sup> solvothermal synthesis,<sup>13</sup> solution phase growth-based on capping reagents,<sup>14</sup> self-assembly<sup>15</sup> and lithography.<sup>16</sup> These techniques require multiple processing steps and a controlled environment, which limit their large scale application. Therefore, a new powder processing-based technique capable of providing ferroelectric perovskite structures of a high aspect ratio morphology is highly desired.

Furthermore, current generations of ferroelectric devices and resonators are fabricated mainly using lead-based ferroelectric compositions. However, there is growing environmental concern in the use of lead, which has prompted research in to alternative lead-free compositions. The present work addresses both these issues and demonstrates the molten salt synthesis of lead-free  $\text{Na}_{0.5}\text{Bi}_{0.5}\text{TiO}_3\text{--BaTiO}_3$  (NBTBT) ferroelectric whiskers through a topochemical transformation using  $\text{Na}_2\text{Ti}_6\text{O}_{13}$  as a host structure. This technique is highly cost-effective and can provide large quantities of lead-free NBTBT whiskers with a controlled morphology at a relatively low synthesis temperature.<sup>17,18</sup> The topochemical reaction involves the introduction of guest species (ions) in to a host structure resulting in a product with a different structure, but with a morphology similar to that of guest structure. In previous work, this method has been successfully used for the synthesis of shape anisotropic  $\text{ABO}_3$ -type perovskites using Aurivillius type  $\text{PbBi}_4\text{Ti}_4\text{O}_{15}$  and  $\text{Bi}_4\text{Ti}_3\text{O}_{12}$  oxides as the host structures.<sup>19,20</sup>

$\text{Na}_{0.5}\text{Bi}_{0.5}\text{TiO}_3$  is a well known lead-free ferroelectric material. Solid solution of  $(\text{Na}_{0.5}\text{B}_{0.5}\text{TiO}_3)_{(1-x)}\text{--}(\text{BaTiO}_3)_x$  (NBTBT) exhibits a morphotropic phase boundary (MPB) for  $x = 0.05\text{--}0.08$  providing enhanced piezoelectric properties.<sup>21</sup> We optimized the composition near the MPB of the  $(\text{Na}_{0.5}\text{B}_{0.5}\text{TiO}_3)_{(1-x)}\text{--}(\text{BaTiO}_3)_x$  (ref. 22) system and selected  $x = 0.07$  for the synthesis of NBTBT whiskers (hereafter, whiskers having the composition  $(\text{Na}_{0.5}\text{B}_{0.5}\text{TiO}_3)_{(1-x)}\text{--}(\text{BaTiO}_3)_x$  with  $x = 0.07$  will be denoted as NBTBT). In the MPB region, both tetragonal and rhombohedral phases co-exist as the space group symmetry of these two ferroelectric phases is not connected by a direct group theoretical correlation.<sup>23</sup> The piezoelectric/ferroelectric materials at MPB are characterized by an enhanced piezoelectric response. The

<sup>a</sup>Center for Energy Harvesting Materials and Systems (CEHMS), Bio-Inspired Materials and Devices Laboratory (BMDL), Virginia Tech, Blacksburg, VA 24061, USA. E-mail: mauryad@vt.edu

<sup>b</sup>Department of Physics, Central Michigan University, Mount Pleasant, MI 48859, USA

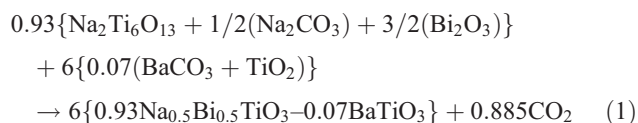
<sup>c</sup>Department of Physics and Institute for Functional Nanomaterials, University of Puerto Rico, San Juan, Puerto Rico, 00931-3343

enhancement in the piezoelectric properties at the MPB has been attributed to increased spontaneous polarization and near degeneracy of the tetragonal and rhombohedral states, which facilitates domain orientation under an applied electric field.<sup>24</sup>

The structural and morphological characterizations of NBTBT whiskers were performed using high-energy X-ray diffraction (XRD) and scanning electron microscopy to elucidate the phase, grain size and grain boundary morphology. Furthermore, HRTEM analysis was used to understand the change in the local microstructure and the mechanism of the topochemical transformation to lead-free NBTBT whiskers. The high temperature behavior and morphological changes of these lead-free NBTBT whiskers were investigated to elucidate the role of the surface energy.

## Experimental

Na<sub>2</sub>Ti<sub>6</sub>O<sub>13</sub> (NTO) whiskers were synthesized by the molten salt synthesis method.<sup>25</sup> The molten salt synthesis method is suitable for realizing crystallites of complex oxides with shape anisotropy at low temperatures and with smaller reaction times due to the enhanced diffusion of reactants in molten salts.<sup>19</sup> In this method, the starting materials are mixed together with a suitable salt (NaCl in the present case) and heated at a temperature higher than the melting point of the salt. After completion of the reaction, the product is washed several times with hot deionized water to remove the salt. In our case, stoichiometric amounts of Na<sub>2</sub>CO<sub>3</sub> and TiO<sub>2</sub> (rutile) powders were ball-milled for 24 h in a polyethylene bottle with yttria-stabilized ZrO<sub>2</sub> balls as the milling media and high purity ethanol as the solvent. The resulting slurry was dried in an oven at 80 °C for 6 h. This dried mixture was mixed with controlled amounts of NaCl followed by ball milling for 24 h to achieve homogeneous mixing. After drying, the homogeneous mixture was crystallized at 1100 °C for 2 h in a covered platinum crucible with a heating and cooling rate of 5 °C min<sup>-1</sup>. The resulting product was washed several times with hot deionized water to achieve NTO whiskers without a trace of salt. Various combinations of oxide to salt ratios (1 : 1, 1 : 2 and 1 : 3) were investigated; however, 1 : 2 ratios were found to provide a high aspect ratio of the host NTO whiskers. The concentration of the host matrix powder and whiskers for the MPB composition of lead-free (Na<sub>0.5</sub>Bi<sub>0.5</sub>TiO<sub>3</sub>)<sub>(1-x)</sub>–(BaTiO<sub>3</sub>)<sub>x</sub> with *x* = 0.07 (denoted as NBTBT) was calculated using the chemical reaction as follows:



Stoichiometric amounts of oxide powders were mixed in 1 : 2 weight ratios with the salt and stirred for 6 h at room temperature (RT) in ethanol to ensure proper mixing. This mixture was dried in an oven for 24 h, followed by heating (heating rate: 5 °C min<sup>-1</sup>) in a covered platinum crucible at 200, 500, 600, 700, 800 and 900 °C for 2 h followed by cooling (cooling rate: 5 °C min<sup>-1</sup>) to RT. All the high temperature experiments were done in a Nabertherm muffle furnace. The resulting whiskers were washed with deionized water several times and dried at 80 °C

for 24 h in an oven. XRD experiments (Cu K $\alpha$  radiation) were conducted on these whiskers to confirm the formation of the perovskite phase at RT using a PANalytical X'Pert Pro powder X-ray diffractometer at an operating voltage of 45 kV and a current of 40 mA. The morphological investigations were performed using a Zeiss LEO 1550 scanning electron microscope at a 5 kV accelerating voltage. In order to record the SEM image, NBTBT whiskers were dispersed on a platinized silicon substrate followed by a conductive gold–palladium coating. HRTEM analysis was performed using a FEI Titan 80–300 transmission electron microscope. For the TEM analysis, the whiskers were mixed with G<sub>2</sub>-epoxy (Gatan Inc.) and then filled into brass tubes of 3 mm in diameter. The tubes were then sliced into thin sections that were mechanically polished. Finally, dimple grinding followed by Ar ion milling was performed to obtain TEM transparent foils.

Room temperature micro Raman studies were conducted in the backscattering geometry using a Jobin-Yvon T6400 Triplemate instrument utilizing laser radiation of 514.5 nm from a coherent Innova 99 Argon source. The green laser light was focused to a  $\sim 2$   $\mu\text{m}$  diameter using a Raman microprobe with a 50 $\times$  objective. A charge-coupled device (CCD) system collected and processed the scattered light. The integration time of the spectrum and the slit width and laser beam power were adjusted in order to achieve a high signal-to-noise ratio. The typical spectral resolution for the Raman system with 1800 grooves per mm grating and 1 in the CCD was less than 1 cm<sup>-1</sup>. The system was calibrated using a Si spectra at room temperature before and after recording the sample spectra. Raman spectra of all the samples were taken at different geometrical positions; the results presented here were the same throughout the matrix.

## Results and discussion

Fig. 1 shows the powder diffraction patterns of the pure NTO matrix and products of the chemical reaction (see eqn (1)) carried out at different temperatures (in °C). The data was taken with Ag K $\alpha$  radiation ( $\lambda = 0.56$  Å) up to Bragg angles,  $2\theta$ , of 120°; *i.e.*, to wave vectors  $q = 4\pi\sin(\theta)/\lambda$  of approximately 20 Å<sup>-1</sup>. Only the range of XRD data up to  $2\theta = 80^\circ$  is shown here for the sake of clarity. The XRD patterns for pure NTO and NBTBT obtained at 800 °C show sharp Bragg peaks indicating good crystallinity. The Bragg peaks in the XRD patterns of the reaction products (*e.g.* the sample treated at 200 °C) are very broad indicating a low degree of crystallinity. This data was then reduced to the atomic pair distribution functions (PDFs) shown in Fig. 2. According to recent studies, high-energy XRD and atomic PDF analyses are very suitable for studying materials structured at the nanoscale.<sup>26</sup> The experimental PDFs peak at real space distances, where well defined atomic coordination spheres exist in the material under study, can be easily used to test and refine structural models. Fig. 2 depicts the atomic pair distribution functions  $G(r)$  (solid line in black) extracted from the full  $2\theta$  range of the XRD patterns shown in Fig. 1. The pair distribution functions (PDFs) for pure NTO and NBTBT (800 °C) show a series of well-defined peaks at high interatomic distances reflecting the presence of a sequence of well-defined coordination spheres in these crystalline materials. These PDFs

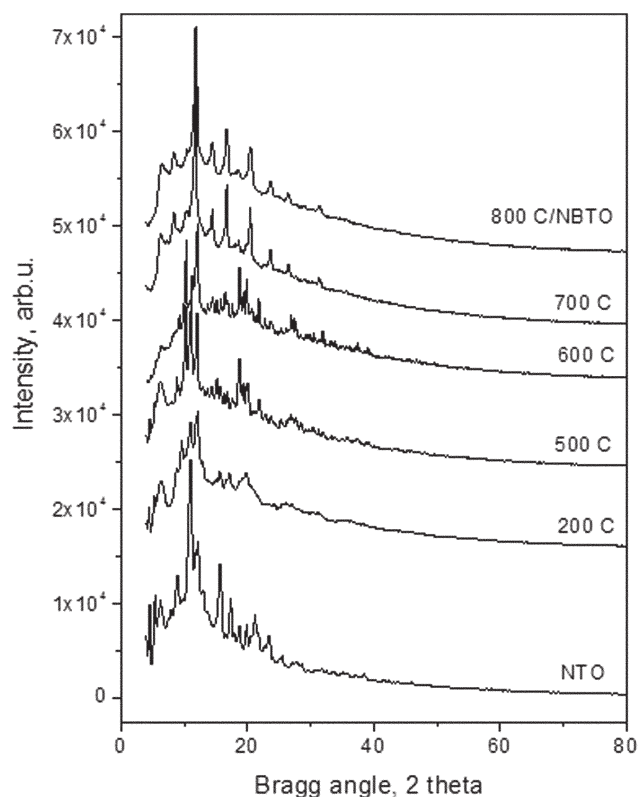


**Fig. 1** Powder diffraction patterns of the pure NTO matrix and the products of its reaction (see eqn (1)). The experiment was conducted at different temperatures (in °C) in an increasing order to understand the transformation sequence. Note that the XRD patterns of pure NTO and NBTBT obtained at 800 °C show sharp Bragg peaks indicating good crystallinity. The Bragg peaks in the XRD patterns of the reaction products (e.g. samples treated at 200 and 500 °C) are very broad indicating a low degree of crystallinity.

of the starting and ending products of the reaction are very well approximated with the structure models (dotted line in red), which feature the monoclinic (S.G.  $C2/m$ ) and rhombohedral (S.G.  $R3c$ ) structures of crystalline  $\text{Na}_2\text{Ti}_6\text{O}_{13}$  (NTO, JCPDS #460001) and  $\text{Na}_{0.5}\text{Bi}_{0.5}\text{TiO}_3$  (NBT, JCPDS #850530), respectively. The PDFs of the samples treated at 200 °C show only a few peaks at relatively low interatomic distances reflecting a poor crystalline state. Crystallinity improves with an increase in the reaction temperature as manifested by the increased sharpness of the peaks in the PDFs of the samples treated at temperatures higher than 200 °C.

Fig. 3 shows the schematics of the fragments from the structures of NTO and NBTBT.  $\text{TiO}_6$  octahedra are shown in blue and Na/Bi/Ba atoms are shown in yellow. Several of the interatomic distances between connected  $\text{TiO}_6$  octahedra are marked with arrows. The low- $r$  part of the experimental atomic PDFs of Fig. 2 is depicted in Fig. 4. The arrows mark several distances between the atoms sitting on the vertices of the corner sharing  $\text{TiO}_6$  units (see Fig. 3) that exist in NTO and persist in the products of its reaction (see eqn (1)) until a lead-free perovskite NBTBT is formed. This result indicates the existence of a topochemical relationship between NTO and lead-free NBTBT. These kind of layered titanates have been found to be suitable precursors for framework perovskites in other studies as well.<sup>27</sup>

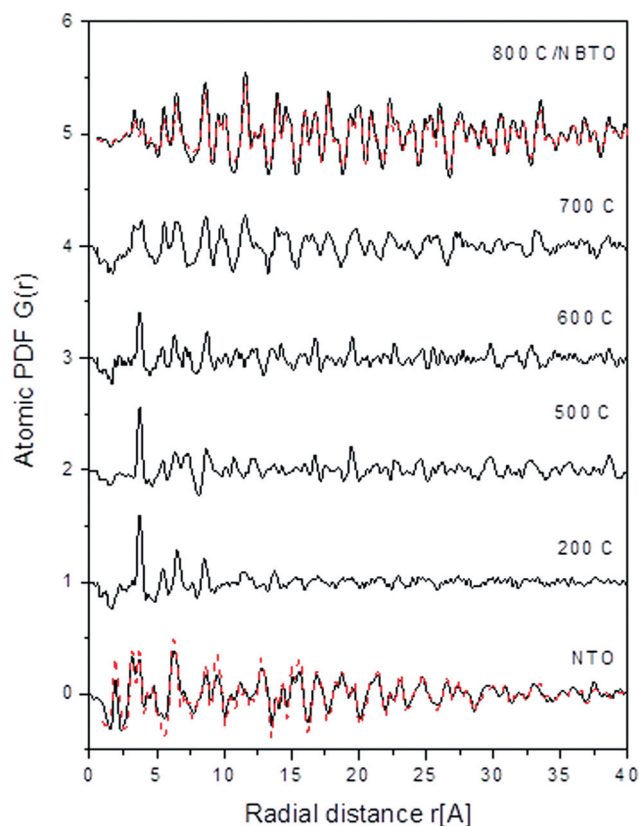


**Fig. 2** Atomic pair distribution functions,  $G(r)$  (full line in black), extracted from the full  $2\theta$  range of the XRD patterns shown in Fig. 1. The PDFs for the starting NTO and resulting NBTBT are very well approximated with the structure models (broken line in red), which feature the monoclinic (S.G.  $C2/m$ ) and rhombohedral (S.G.  $R3c$ ) structures of crystalline  $\text{Na}_2\text{Ti}_6\text{O}_{13}$  (NTO) and  $\text{Na}_{0.5}\text{Bi}_{0.5}\text{TiO}_3$  (NBT), respectively.

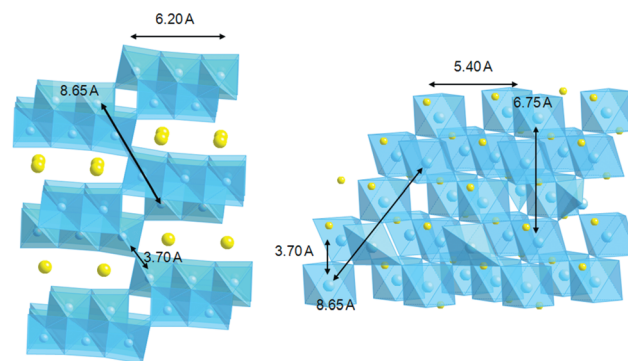


**Fig. 3** A schematic of the fragments from the structures of NTO (left) and NBTBT (right).  $\text{TiO}_6$  octahedra are shown in blue and Na/Bi atoms are shown in yellow. Several interatomic distances between connected  $\text{TiO}_6$  octahedra are marked with arrows.

Fig. 5(a) shows the XRD pattern of the  $\text{Na}_2\text{Ti}_6\text{O}_{13}$  (NTO) whiskers taken with Cu  $K\alpha$  radiation, which allows a better resolution in reciprocal space. The data confirms that these whiskers crystallize in a monoclinic phase (JCPDS #460001). Fig. 5(b) and (c) show the Cu  $K\alpha$  XRD patterns of NBTBT whiskers synthesized topochemically at 800 and 900 °C and reveal the

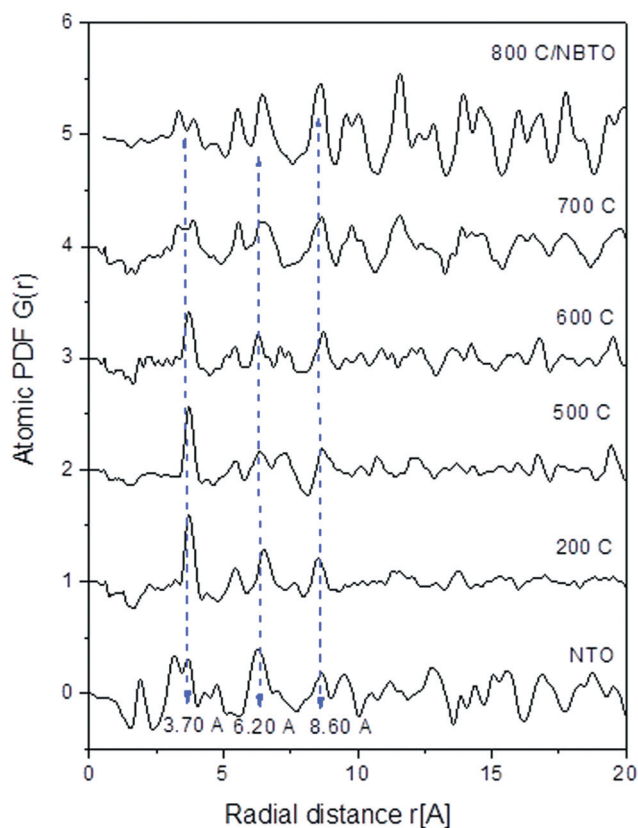


**Fig. 4** The low- $r$  part of the experimental atomic PDFs of Fig. 2. Arrows mark several distances between the atoms sitting on the vertices of corner sharing Ti–O<sub>6</sub> units (see Fig. 3) that exist in NTO and persist in the products of its reaction (see eqn (1)) until a perovskite NBTBT is formed.

formation of a perovskite phase for these whiskers. However, a small impurity peak, marked with ‘\*’ in the XRD-pattern of the sample synthesized at 800 °C, suggests more than 95% transformation occurs at this temperature. A magnified view of the {111}<sub>c</sub> and {200}<sub>c</sub> Bragg peaks for the sample processed at 900 °C is shown in the inset of Fig. 5(c). The subscript c stands for the cubic crystal system. A small shoulder, appearing in the {111}<sub>c</sub> and {200}<sub>c</sub> peaks, indicates that the composition is near the MPB. In order to determine the structural type of the whiskers processed at 900 °C, higher energy XRD patterns were recorded using Ag K $\alpha$  radiation [Fig. 5(d)]. This data was then reduced to an atomic pair distribution function (PDF) shown in Fig. 5(e). The experimental PDF for the whiskers [see Fig. 5(e)] shows well defined peaks at high real space distances. The PDF peaks decay to zero at distances of about 10–15 nm, which may be considered to be the length of structural coherence, also known as the crystallite domain size, in this material. These XRD/PDF results indicate that the larger grains observed in these whiskers by SEM (discussed later in this article) are made of relatively small size crystallites. Furthermore, the data in Fig. 5(f) shows that the PDF can be well fitted with a model based on the rhombohedral structure JCPDS (#850530) of the NBT perovskite<sup>28</sup> confirming that the whiskers are a single phase ferroelectric material.

Fig. 6 shows the Raman spectra of the NTO matrix and of specimens after reaction at different temperatures (in °C). The

Raman spectra of pure NTO and the sample processed at 200 °C are similar indicating no change in the structure of NTO. The peaks observed in the Raman spectra of NTO in the present study are similar to those reported previously.<sup>29</sup> The Raman spectra of NTO depict modes at 276 and 334 cm<sup>-1</sup> due to vibration of Na–O–Ti (ref. 30). The Raman modes in the region of 600–700 cm<sup>-1</sup> have been attributed to the Ti–O–Ti stretch in the edge shared octahedra. However, the mode observed at 743 cm<sup>-1</sup> is characteristic of corner sharing octahedra in NTO (ref. 31). The mode at 872 cm<sup>-1</sup> was attributed to short Ti–O bonds in the distorted TiO<sub>6</sub> octahedra of NTO (ref. 32). Furthermore in the specimen processed at 500 °C and at higher temperatures, Bi and Ba start diffusing inside the system in the presence of the molten salt. This can be seen in terms of the new bands that appeared at 55 cm<sup>-1</sup> and the peak around 91 cm<sup>-1</sup> (observed in NTO), which becomes asymmetric indicating a shoulder peak. Another small peak appeared as a shoulder on the main peak observed at 137 cm<sup>-1</sup>. At 600 °C, the increase in the intensity of the band observed at 55 cm<sup>-1</sup> was noticed and the peaks at about 91 cm<sup>-1</sup> and 137 cm<sup>-1</sup> gave rise to a doublet, which was attributed to the increased inharmonicity of the vibration and a change in the local symmetry due to the substitution of heavier Bi in the Na site. The decrease in the intensity of the various peaks below 200 cm<sup>-1</sup> could be a result of the substitution of Bi and Ba at the Na site. However, the effect of the substitution of Ba would be smaller due to its smaller concentration. A mode at 276 cm<sup>-1</sup> becomes broad and diffuse indicating the appearance of two more peaks for samples processed at 600 °C, which appears to be perturbation in the Na–O–Ti vibrations due to the Na site substitution. A noticeable change occurs in the intensity of the Raman peak at 525 cm<sup>-1</sup>, which increases with the reaction temperature. The bands in the range of 400–600 cm<sup>-1</sup> are attributed to the bending motion of the TiO<sub>6</sub> octahedra.<sup>33</sup> Therefore, the increase in the intensity of the peak at about 525 cm<sup>-1</sup> with the reaction temperature could be attributed to the enhanced TiO<sub>6</sub> bending motion in the transformation process from the TiO<sub>6</sub> octahedra edge sharing to the corner (vertex) sharing. Moreover, with an increase in the reaction temperature, a gradual decrease in the intensity of the modes appearing within the 657–680 cm<sup>-1</sup> region could be interpreted as a loss of the edge sharing coordination that is prevailing in the NTO-type system (see Fig. 3a). The decrease in the intensity of the mode observed at 748 cm<sup>-1</sup> is likely to be due to the Ti–O–Ti corner sharing coordination. It shows subtle changes with an increase in the reaction temperature. However, this band appears to still be present, although buried under a broader band, in the region of 700–850 cm<sup>-1</sup> in the Raman spectra observed for the 700, 800 and 900 °C treated samples. The persistence of the modes observed in the higher wavenumber region of 700–850 cm<sup>-1</sup>, which are attributed to the corner-shared TiO<sub>6</sub> octahedra, also suggests a topochemical-type conversion in line with the results of the high-energy XRD and PDF analysis. The poorly resolved Raman spectra of the specimens processed at 700 °C resembles a density of states spectrum because the disorder due to the random distribution of Na, Bi and Ba ions breaks the  $k = 0$  selection rule and permits phonons from the entire Brillouin zone to become Raman active. The Raman spectra of the specimen processed at 800 and 900 °C are similar to those previously reported for an NBT-based system (space

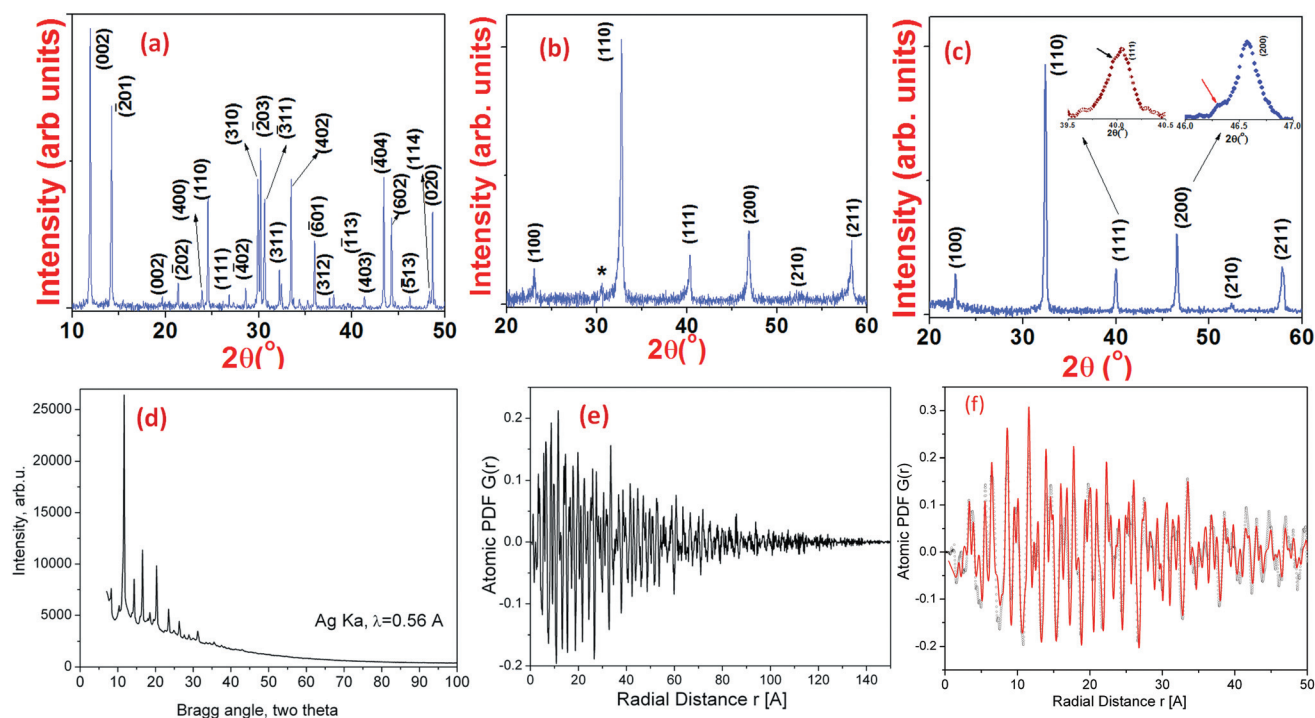


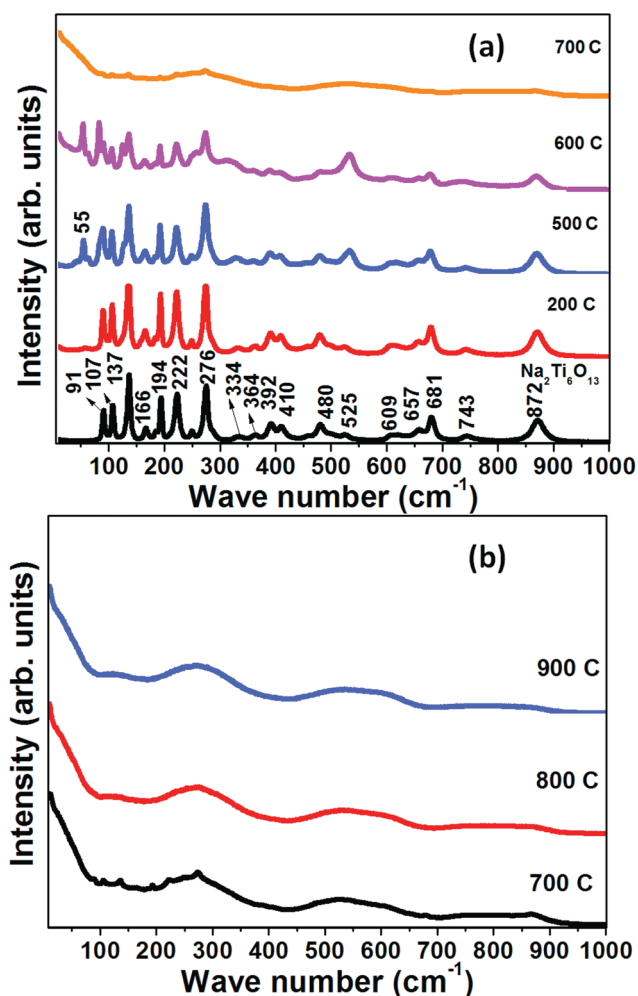
**Fig. 5** Cu  $K\alpha$  X-ray diffraction data at RT for (a) NTO powder whiskers with monoclinic symmetry, (b) NBTBT processed at 800 °C and indexed with reference to the cubic phase, (c) NBTBT processed at 900 °C with an inset depicting the magnified view of the  $\{111\}_c$  and  $\{200\}_c$  reflections, where c stands for the cubic phase. The high energy X-ray diffraction data of NBTBT/900 °C (d) and the respective atomic PDF (e). The low- $r$  part of the experimental PDF data is shown in Fig. 5f (open circles). The data can be fitted very well with the structure model (line in red) based on the rhombohedral (S.G.  $R3c$ ) structure of the NBT perovskite.

group  $R3c$  ( $C_{3v}^6$ ) with broad modes due to the local disorder in the structure.<sup>34</sup> This confirms the successful transformation of NTO, which is made of mostly edge sharing octahedra, to the lead-free NBTBT system, which is made of corner sharing octahedra (see Fig. 3(a) and (b), respectively).

Fig. 7(a) shows the morphology of  $\text{Na}_2\text{Ti}_6\text{O}_{13}$  whiskers prepared using the molten salt synthesis method at 1100 °C. Fig. 7 (b)–(d) show the micrographs of the ferroelectric NBTBT whiskers synthesized at 700, 800 and 900 °C, respectively. It can be clearly seen from these micrographs that, despite the structural transformation, the overall morphology of the whiskers is maintained up to 900 °C. For the sake of clarity, the magnified view of the surface morphologies of the whiskers treated at various temperatures is presented in Fig. 8(a)–(f). As can be seen in this figure, the lead-free NBTBT whiskers processed at 900 °C (Fig. 8(f)) are composed of densely packed grains revealing their polycrystalline nature. However, this kind of grain growth in the sample processed at a relatively low temperatures (<900 °C) is not very obvious. Still, the surface clearly shows a change in morphology (Fig. 8) due to the diffusion of  $\text{Ba}^{2+}$  and  $\text{Bi}^{3+}$  during the reaction. NTO with tunnel structures (see Fig. 3 (a)) have excellent ion exchange properties and the  $\text{Na}^+$  atom can be easily replaced by  $\text{Ba}^{2+}$  and  $\text{Bi}^{3+}$ . The presence of these ions with a higher positive charge further facilitates the structural transformation from NTO to lead-free NBTBT. The estimated grain size on the NBTBT whiskers after reaction at 900 °C was found to be in the range of 100–500 nm (Fig. 8(f)). In order to analyze the local microstructure and identify the phase content at

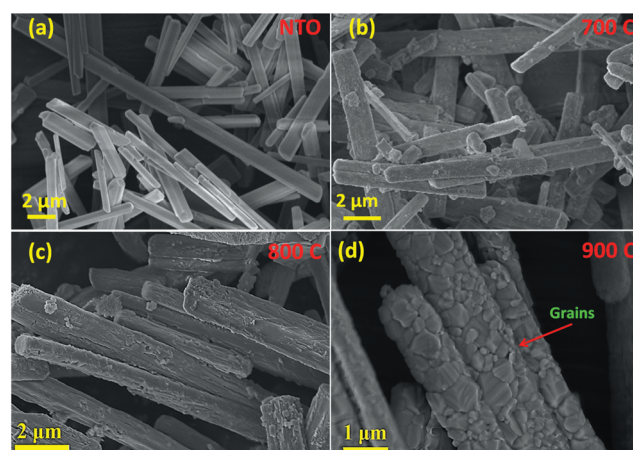
the various stages of thermal processing, HRTEM was performed.

Fig. 9(a) shows the lattice fringes of  $\text{Na}_2\text{Ti}_6\text{O}_{13}$  whiskers viewed along the  $[010]_M$  zone axis, where the subscript M stands for a monoclinic system. The  $\{001\}_M$  planes parallel to the length of the whiskers were found to run along the growth direction. Fig. 9(b)–(d) show the HRTEM image of the sample processed at 800 °C. EDS analysis conducted on the edge marked 'A' and towards the core marked 'B' in Fig. 9(b) shows an atomic % ratio of Na/Ti = 13.3 and 1.50, respectively. This indicates that during the topochemical reaction, Na ions diffuse outward. At the same time, Ba and Bi ions diffuse inside the whiskers due to difference in the chemical potential.<sup>35</sup> This results in a rearrangement of the octahedral building blocks as explained in the forthcoming paragraph. A lattice image showing the atomic planes with an interplanar spacing  $\sim 0.80$  nm from the vicinity of the region marked with B on Fig. 9(b) is shown in Fig. 9(c). The interplanar spacing is smaller than  $d_{001} \sim 0.903$  nm of the host  $\text{Na}_2\text{Ti}_6\text{O}_{13}$  matrix. This change in the interplanar spacing is expected due to the outward diffusion of Na atoms from the core of the sample and the concomitant inward diffusion of Bi/Ba atoms. This state can be related to a transient intermediate phase. Since this ion exchange is carried out in a molten salt and is of a topochemical type, it can produce a metastable intermediate state, which is otherwise inaccessible with high temperature reactions.<sup>36</sup> Moreover, molten salt (NaCl) provides a strong oxidizing atmosphere, which helps to stabilize the higher oxidation state of  $\text{Ti}^{4+}$  in the system. The area towards the



**Fig. 6** (a) Raman spectra of the pure NTO matrix and the products of its reaction (see eqn (1)). The syntheses were conducted in the temperature range of 200–700 °C. The Raman spectrum of NTO and the specimen processed at 200 °C are similar. Note the systematic changes in the intensity of various peaks in the spectra of the specimens reacted at and above 500 °C. (b) Raman spectra of samples reacted at 700, 800 and 900 °C. The spectra of the specimen reacted at 800 °C and 900 °C are similar to the typical Raman scattering behavior observed in NBT-based systems.

edge marked A in Fig. 9(b) is enlarged in Fig. 9(d). The lattice fringes, with planes of various orientations, can be observed showing a polycrystalline transient state and nucleation sites. The planes are marked with arrows and the area near the arrow head is magnified in the small figures next to Fig. 9(d). The edge-type dislocation marked in the magnified figure of “region 3” acts as a potential site for nucleation and growth of the grains.<sup>37</sup> Thus, only partial transformation occurs at 800 °C and further thermal treatment is required to obtain a homogeneous phase. Fig. 9(e) shows the microstructure of the NBTBT whiskers processed at 900 °C for 2 h. The inset image shows the fast Fourier transform (FFT) of the image in Fig. 9(e). The spots in the FFT can be indexed in a monoclinic-type structure (JCPDS #460001). The zone  $[2\bar{2}1]_M$  was obtained by indexing this FFT. Interestingly, the average NBTBT structure obtained by high energy XRD and PDF analysis was found to be of a



**Fig. 7** SEM micrographs of (a) NTO whisker matrix. NBTBT whiskers after reaction at (b) 700 °C, (c) 800 °C and (d) 900 °C. The length of the whiskers varies from 7.0–20 μm and the width varies from 0.30–1.0 μm. The overall shape of the whiskers was maintained, even after reaction at varying high temperatures, but a noticeable change in the surface morphology was observed.

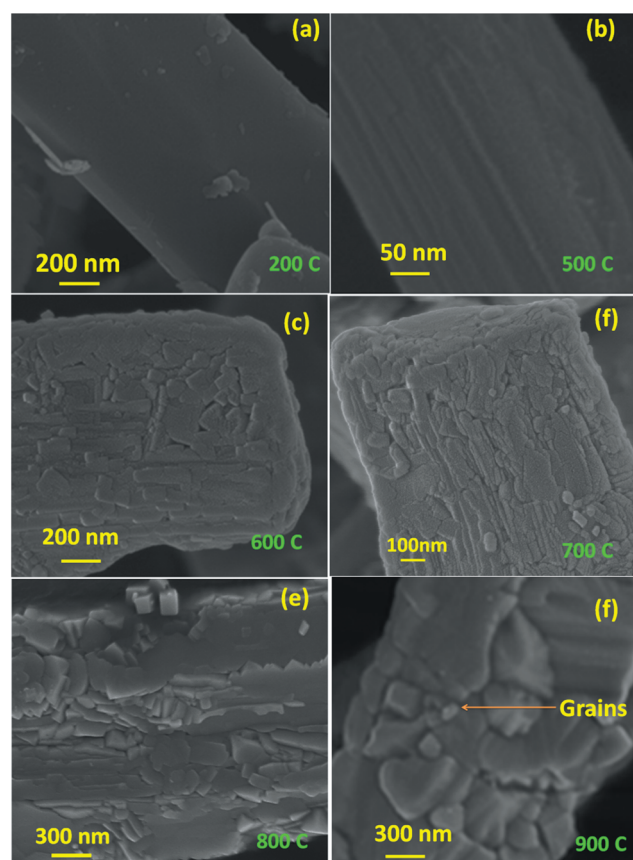


**Fig. 8** Magnified SEM micrographs depicting the morphological changes in the whiskers reacted at (a) 200 °C, (b) 500 °C, (c) 600 °C, (d) 700 °C, (e) 800 °C and (f) 900 °C. Note the effect of the reaction temperature on the surface morphology, which leads to development of nano-size grains at 900 °C.

rhombohedral type. The results indicate the presence of a difference between the local and average lead-free NBTBT structure implying an incommensurate-type modulated structure at the

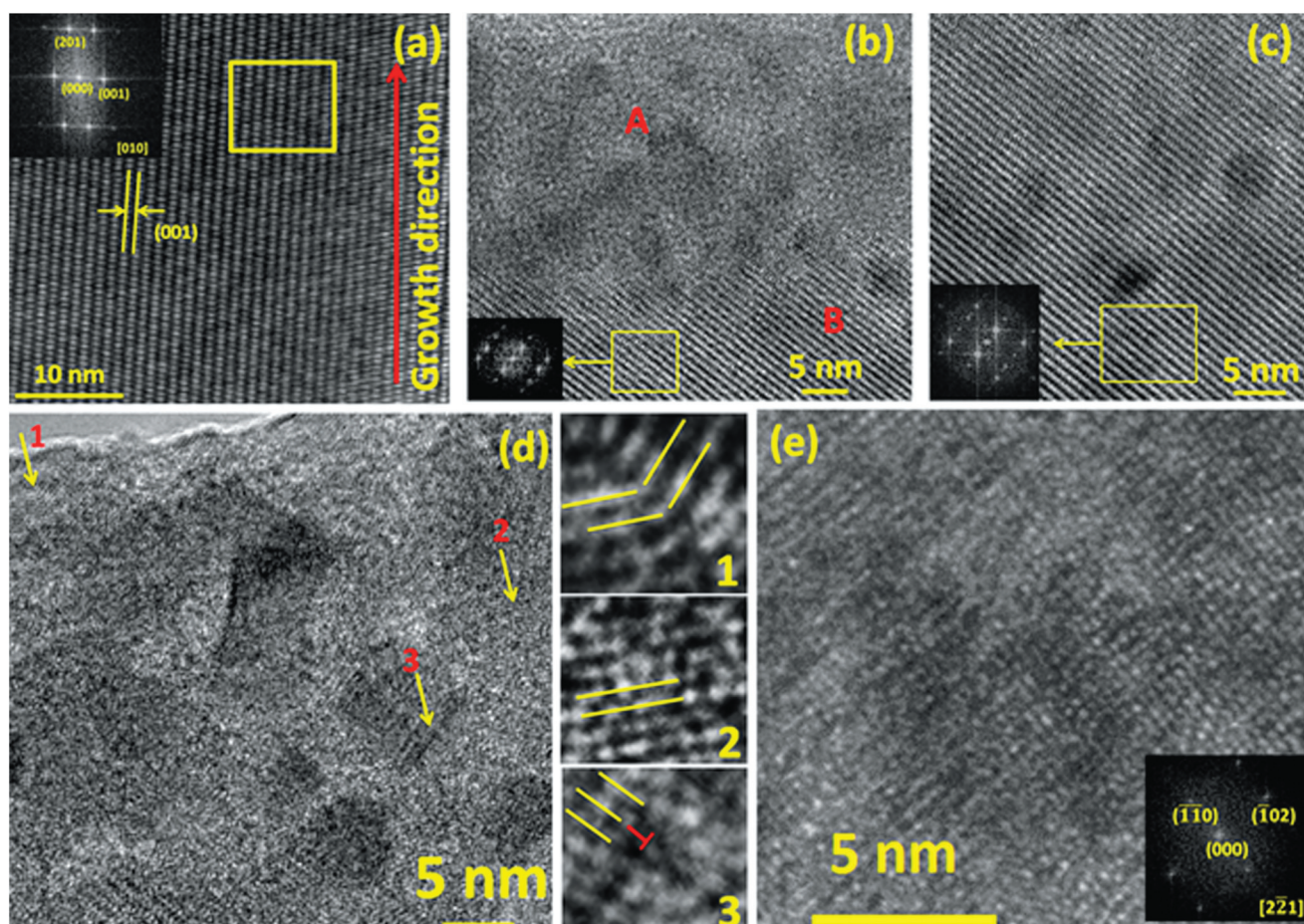


**Fig. 9** The lattice fringe of (a)  $\text{Na}_2\text{Ti}_6\text{O}_{13}$  matrix whiskers synthesized at 1100 °C. (b) An HRTEM image of a NBTBT whisker processed at 800 °C. (c) The lattice fringes corresponding to the region marked as 'B' in (b), which depict the core of the whiskers with larger interplanar spacing than NBT-based systems. (d) The lattice fringes corresponding to region 'A' in (b) near the edge of the NBTBT whisker processed at 800 °C; the regions marked 1, 2 and 3 depict the planes with various orientations on the same whisker and the symbol  $\perp$  is used to depict the edge-type dislocation in (d). (e) The lattice images of the NBTBT whiskers processed at 900 °C.

nano-scale. Furthermore, the intermediate phases with monoclinic distortions are considered to be responsible for the enhanced piezoelectric response in the MPB compositions of lead-based oxide solid solutions, including  $\text{Pb}(\text{Zr}_{1-x}\text{Ti}_x)\text{O}_3$  (PZT), PZN-PT and PMN-PT.<sup>38–40</sup> Various studies employing high energy probing techniques have shown that the local symmetry of the MPB compositions can be different from the average bulk symmetry. In perovskite ferroelectric materials, these local distortions are generally found to be of a monoclinic type.<sup>41,42</sup> Therefore, the observed local monoclinic distortion in NBTBT appears to be main cause of the enhanced ferroelectric/piezoelectric response at the MPB in this system.

The detailed mechanism of the microstructural change and transformation of the NTO host into the  $\text{ABO}_3$ -type NBTBT structure can be summarized as follows: when stoichiometric amounts of the starting materials are mixed with NaCl and heated to 800 and 900 °C, the salt melts and the decomposing  $\text{BaCO}_3$  and  $\text{Bi}_2\text{O}_3$  provide  $\text{Ba}^{2+}$  ions and  $\text{Bi}^{3+}$  ions. These ions react with the host NTO matrix due to difference in the chemical potential, resulting in the formation of an  $\text{ABO}_3$ -type perovskite structure. NTO belongs to the  $\text{M}_2\text{Ti}_n\text{O}_{2n+1}$  family of compounds, where  $n = 6$  or  $3$  and  $\text{M} = \text{Na}$  or  $\text{K}$ . It has a base-centered

monoclinic structure with lattice parameters,  $a = 1.51310$  nm,  $b = 0.37450$  nm,  $c = 0.91590$  nm and  $\beta = 99.3^\circ$  and is of space group  $C2/m$  (ref. 43). The NTO structure is a 3-D network of  $\text{TiO}_6$  octahedra joined by corners and edges resulting in a zig-zag structure (see Fig. 3(a)) with rectangular tunnels along the  $y$ -axis of the monoclinic lattice, where the sodium ions are located. On the other hand, the  $\text{ABO}_3$  perovskite structure features a simple cubic lattice in which the octahedra shares only corners and the B cation is at the origin of the Bravais cell.<sup>44</sup> In the present case, the A site is shared by  $\text{Na}^+/\text{Ba}^{2+}/\text{Bi}^{3+}$  ions and the B site is occupied by  $\text{Ti}^{4+}$ . The transformation process of NTO to NBTBT can be rationalized as follows:

(i) During the synthesis,  $\text{Ba}^{2+}/\text{Bi}^{3+}$  diffuse into the host lattice of  $\text{Na}_2\text{Ti}_6\text{O}_{13}$  through an ion exchange mechanism with  $\text{Na}^+$ , resulting in a rearrangement of the octahedra sharing scheme to minimize the energy and allow for a thermodynamically stable configuration. A schematic of the NTO-to-NBTBT transformation ( $\text{ABO}_3$ -type perovskite) is shown in Fig. 10(a) and the coordination of the octahedra in the perovskite structure is presented in Fig. 10(b). The geometrical connection of the octahedra plays an important role in this transformation. The perovskite structure is composed of corner (vertex) sharing octahedra<sup>45</sup> at

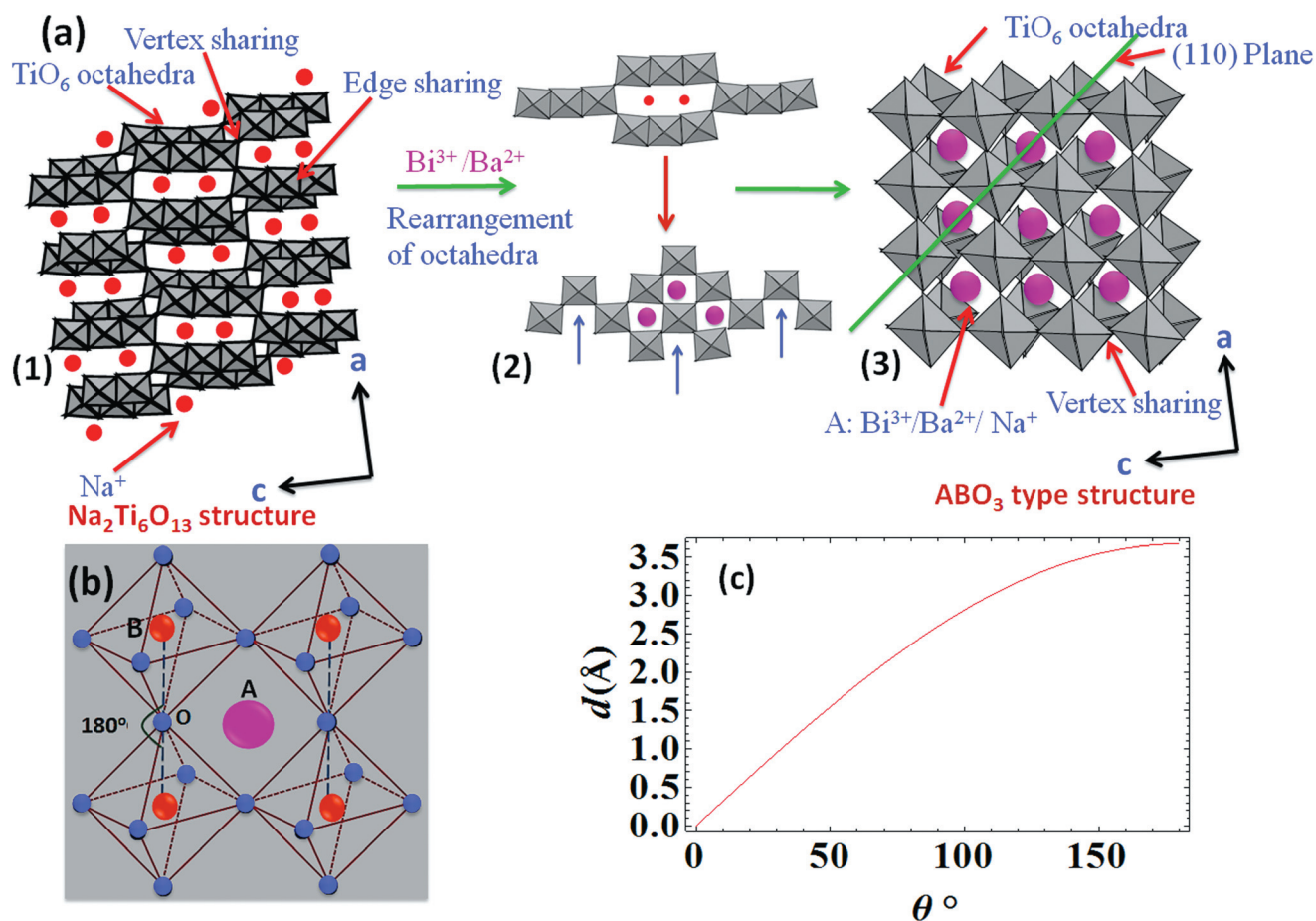


**Fig. 10** (a) A schematic of the transformation of the  $\text{Na}_2\text{Ti}_6\text{O}_{13}$  structure into an  $\text{ABO}_3$ -type perovskite structure (NBTBT) through rearrangement of the octahedral connectivity type. (b) A schematic representation of the perovskite structure ( $\text{ABO}_3$ ). (c) The change in the distance between two Ti-Ti atoms with the tilt angle of the corner sharing octahedra depicting the optimum distance between two Ti-Ti atom at  $180^\circ$ , as in  $\text{ABO}_3$ -type perovskites.

$180^\circ$  and any deviation from this angle decreases the distance between the Ti atoms (Fig. 10(b)), resulting in an increased repulsion potential experienced by the Ti atom and a smaller screening effect from the negative charge of the oxygen atoms. As a result, the free energy of this structural configuration increases and the structure becomes unstable. The equation describing the distance between two Ti-Ti (Fig. 10(b)) atoms can be given as:

$$d = a(\sqrt{2(1 - \cos \theta)}) \quad (2)$$

where  $\theta$  is the angle between the Ti-O-Ti in the corner sharing octahedra and “ $a$ ” is the Ti-O bond length in the Ti-O-Ti bonding bridge between octahedra sharing two vertices. The order parameter  $\eta = 180 - \theta$  has two limiting values of  $180^\circ$  and  $0^\circ$ , where  $\theta$  is the deviation of the bond angle from  $180^\circ$  in the Ti-O-Ti bonding bridge, *i.e.* in the geometrical connection of the vertex sharing octahedra. Therefore, the system will be most stable for  $\eta = 0^\circ$  *i.e.*  $\theta = 180^\circ$ . Fig. 10(c) plots eqn (2) with  $\theta$  ranging from 0 to  $180^\circ$ . However, in reality, the inclination angle can vary from  $131.8^\circ$  to  $180^\circ$  (ref. 45). The bond length ‘ $a$ ’ of Ti-O was taken to be  $2.009 \text{ \AA}$  from the archetype perovskite  $\text{BaTiO}_3$  with a cubic phase<sup>46</sup> as the reaction occurs at high temperature, where most  $\text{ABO}_3$ -type perovskites have a cubic

structure. This plot (see Fig. 10c) shows the change in perpendicular distance between two Ti atoms with the angle between the vertex sharing octahedra. It can be noticed here that this distance is optimal for  $\theta = 180^\circ$ . We can further comprehend the mechanism of rearrangement of  $\text{Na}_2\text{Ti}_6\text{O}_{13}$  into the  $\text{ABO}_3$ -type NBTBT structure as follows: the energy of the edge shared octahedra configuration is higher than that of the corner sharing configuration and, consequently, the edge sharing octahedra are driven into a more energetically favorable coupling scheme during the reaction. According to our model, during the reaction, octahedra with shared edges in  $\text{Na}_2\text{Ti}_6\text{O}_{13}$  move in the  $\{100\}$  direction to achieve the corner sharing connection of the  $\text{ABO}_3$ -type structure. This rearrangement is shown schematically in step 2 of Fig. 10(a) and is supported by the findings of the atomic PDFs analysis that indicates the existence of a relationship between the NTO and NBTO (see Fig. 4 and 5) structures. The arrows marked in step 2 indicate the direction of the translational motion of the octahedra.

(ii) The perovskite structure is isotropic and, therefore, after the topochemical conversion, the sample at a higher temperature exhibits a well-defined grain morphology, which could be understood by assuming Rayleigh-type instability as observed in Fig. 7(d) and 8(f) (ref. 25).

The schematic representation of the  $ABO_3$ -type structure depicted in Fig. 10(b) shows the presence of  $O^{2-}-T^{4+}-O^{2-}$  triples parallel to the  $x$ ,  $y$  and  $z$  axes. Considering the  $ABO_3$ -type perovskite with no center of symmetry, under the application of an electric field along the  $z$  axis, the  $O^{2-}-T^{4+}-O^{2-}$  chains parallel to the  $z$  axis get polarized without a significant effect on the chains parallel to the other two axes. The whisker polarized in the direction of the  $z$  axis imparts ferroelectricity to the system. Moreover, when the configuration of the A site cation suffers a distortion (*i.e.* the A site atom is displaced from its average position) during the displacement of the oxygen ions in the above process, the shape of the unit cell changes resulting in a piezoelectric effect.<sup>45</sup> However, in NBTBT, the distortion would be different for the A site occupied with different atoms ( $Bi^{3+}$ ,  $Ba^{2+}$  or  $Na^+$ ) as they have different charges and ionic radii and this results in disorder in the lattice as has also been indicated by the broad Raman modes.

Furthermore, the NBTBT whiskers were dispersed on an alumina plate and subjected to heat treatment in air at various temperatures for 2 h in order to investigate the high temperature morphological transformation and the role of the surface and grain boundary energies (Fig. 11). Upon heat treatment at 1000 °C, coalescence occurred among the grains of the whiskers as the small grains (Fig. 8(e–f)) that were observed at RT are no longer visible due to the high dihedral angles. A further increase in the temperature leads to the appearance of relatively large grains within the whiskers, which form a bamboo-type structure at 1100 and 1175 °C (Fig. 11(b) and (c)). At 1175 °C, the whisker starts to get thinner in the vicinity of the grain boundaries showing grain boundary grooving as a result of the surface/grain boundary diffusion and a local evaporation–condensation process<sup>47</sup> [Fig. 11(c)]. According to Mullins' model:<sup>48</sup>  $\gamma_b = 2\gamma_s \sin \theta$ , where  $\gamma_b$  and  $\gamma_s$  are the grain boundary and surface energy, respectively, and  $\theta$  is the surface inclination at the root of the groove (Fig. 11(c)). In the present case,  $\theta$  is measured from

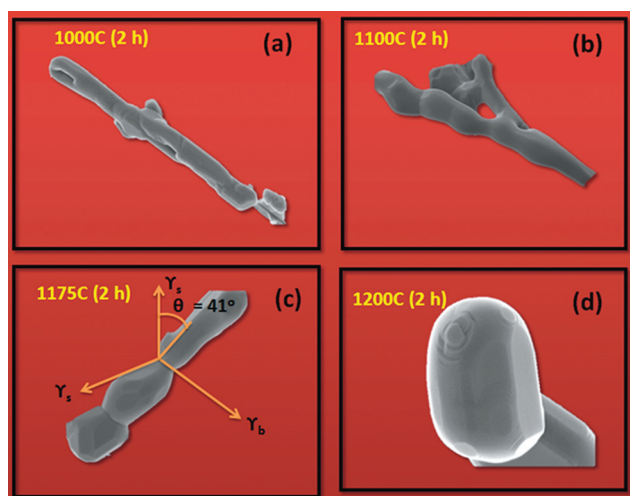


**Fig. 11** The change in the morphology of the isolated whiskers heated on an alumina plate in air at various temperatures (a) 1000 °C, (b) 1100 °C, (c) 1175 °C and (d) 1200 °C. The higher grain boundary energy leads to the disintegration of the whiskers to achieve the equilibrium cubical shape.

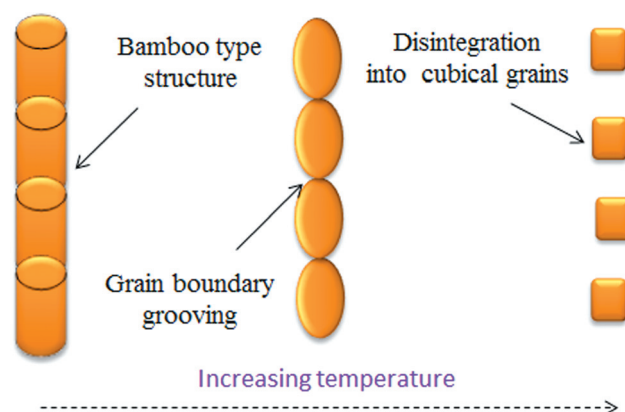


**Fig. 12** A schematic representation of the change in the morphology during disintegration of the NBTBT whisker with an increase in temperature. The polycrystalline whisker disintegrates into isolated cubic grains *via* grain boundary grooving and Rayleigh-type instability.

the SEM micrograph (Fig. 11(c)) and is found to be 41° and, therefore,  $\gamma_b/\gamma_s$  equals 1.31. Thus, the system has an unusually higher grain boundary energy compared to the surface energy. As a result, upon further heating at 1200 °C, the whiskers eventually disintegrate into individual grains, which is in close analogy with Rayleigh-type instability<sup>47,49,50</sup> so that the grain boundary energy is minimized by thermal grooving; *i.e.*, grain boundary grooving (Fig. 11(d)) to achieve an equilibrium cubical shape of the grain. Rayleigh-type instability was originally developed to explain the breaking of liquid jets into small droplets but has since been used to explain phenomena such as the disintegration of nanowires into small beads<sup>51</sup> and the fission of charged finite systems, such as atomic nuclei or liquid droplets.<sup>52</sup> Grain boundary grooving and Rayleigh-type instability could both lead to the disintegration of polycrystalline whisker with the bamboo-type structure, as both these mechanisms are driven by surface energy.<sup>53</sup> However, in the present case, grain boundary grooving is considered to be the dominant mechanism. Fig. 12 depicts a schematic representation of the disintegration of lead-free NBTBT whiskers into isolated cubical grains.

## Conclusions

The reaction route adopted in this work allows the topochemical conversion and structural rearrangement *via* translation of the edge shared octahedra of the starting NTO material, which leads to the formation of nanostructured  $Na_{0.5}B_{0.5}TiO_3$ – $BaTiO_3$  (NBTBT) ferroelectric whiskers. These whiskers have a rhombohedral-type average structure of the perovskite phase indicating their ferroelectric nature as confirmed by high energy X-ray diffraction coupled with pair distribution function (PDF) analysis and Raman scattering. High-resolution transmission microscopic (HRTEM) analysis reveals a local monoclinic structural distortion of the NBTBT whiskers suggesting the presence of a modulated structure at the nanoscale. Upon high temperature treatment, morphological changes take place resulting in breaking of the whiskers into individual grains as a consequence of a thermal grooving effect driven by minimization of the higher grain boundary energy. The lead-free NBTBT ferroelectric

whiskers have potential applications in environmentally benign microelectronic devices.

## Acknowledgements

The authors gratefully acknowledge financial support from National Science Foundation (synthesis and property measurements) and the Office of Basic Energy Science, Department of Energy (microscopy analysis). The authors would also like to thank NCFL and VT for their help with the characterization.

## References

- 1 M. E. Lines and A. M. Glass, *Principles and Applications of Ferroelectrics and Related Materials*, Clarendon, Oxford, UK, 1977.
- 2 J. F. Scott and C. A. Paz de Araujo, *Science*, 1989, **286**, 1400–1405.
- 3 S. O'Brien, L. Brus and C. B. Murray, *J. Am. Chem. Soc.*, 2001, **123**, 12085–12086.
- 4 C. Liu, B. Zou, A. J. Rondinone and Z. J. Zhang, *J. Am. Chem. Soc.*, 2001, **123**, 4344–4345.
- 5 B. Jiang, J. L. Peng, L. A. Bursill and W. L. Zhong, *J. Appl. Phys.*, 2000, **87**, 3462–3467.
- 6 M. Alexe, C. Harnagea, W. Erfurth, D. Hesse and U. Gösele, *Appl. Phys. A: Mater. Sci. Process.*, 2000, **70**, 247–251.
- 7 S. A. Morin, M. J. Bierman, J. Tong and S. Jin, *Science*, 2010, **328**, 476–480.
- 8 Y. Xia, P. Yang, Y. Sun, Y. Wu, B. Mayers, B. Gates, Y. Yin, F. Kim and H. Yan, *Adv. Mater.*, 2003, **15**, 353–389.
- 9 H. Q. Cao, Y. Xu, J. M. Hong, H. B. Liu, G. Yin, B. L. Li, C. Y. Tie and Z. Xu, *Adv. Mater.*, 2001, **13**, 1393–1394.
- 10 Y. J. Zhang, N. L. Wang, S. P. Gao, R. R. He, S. Miao, J. Liu, J. Zhu and X. Zhang, *Chem. Mater.*, 2002, **14**, 3564–3568.
- 11 Y. Y. Wu and P. D. Yang, *J. Am. Chem. Soc.*, 2001, **123**, 3165–3166.
- 12 M. S. Gudiksen and C. M. Lieber, *J. Am. Chem. Soc.*, 2000, **122**, 8801–8802.
- 13 X. Wang and Y. Li, *J. Am. Chem. Soc.*, 2002, **124**, 2880–2881.
- 14 X. G. Peng, L. Manna, W. D. Yang, J. Wickham, E. Scher, A. Kadavanich and A. P. Alivisatos, *Nature*, 2000, **404**, 59–61.
- 15 C. Pacholski, A. Kornowski and H. Weller, *Angew. Chem., Int. Ed.*, 2002, **41**, 1188–1191.
- 16 Y. Yin, B. Gates and Y. Xia, *Adv. Mater.*, 2000, **12**, 1426–1430.
- 17 M. Granahan, M. Holmes, W. A. Schulze and R. E. Newnham, *J. Am. Ceram. Soc.*, 1981, **64**, C68–C69.
- 18 C. C. Li, C. C. Chiu and S. B. Desu, *J. Am. Ceram. Soc.*, 1991, **74**, 42–47.
- 19 Y. Seno and T. Tani, *Ferroelectrics*, 1999, **224**, 365–372.
- 20 S. F. Poterala, R. J. Meyer Jr and G. L. Messing, *J. Am. Ceram. Soc.*, 2011, **94**, 2323–2329.
- 21 T. Takenaka, K. Maruyama and K. Sakata, *Jpn. J. Appl. Phys.*, 1991, **30**, 2236–2239.
- 22 D. Maurya, C.-W. Ahn and S. Priya, *Advances in Electroceramic Materials II*, 2010, **221**, 47–54.
- 23 W. Cao and L. E. Cross, *Phys. Rev. B: Condens. Matter*, 1993, **47**, 4825.
- 24 A. J. Bell, *J. Mater. Sci.*, 2006, **41**, 13–25.
- 25 D. Maurya, M. Murayama and S. Priya, *J. Am. Ceram. Soc.*, 2011, **94**, 2857–2871.
- 26 V. Petkov, *Mater. Today*, 2008, **11**, 28–38.
- 27 M. Gateshki, S. Yin, Y. Ren and V. Petkov, *Chem. Mater.*, 2007, **19**, 2512–2518.
- 28 S. B. Vakhrushev, B. G. Ivanitskii, B. E. Kvyatkovskii, A. N. Maistrenko, R. S. Malysheva, N. M. Okuneva and N. N. Parfenova, *Fiz. Tverd. Tela (Leningrad)*, 1983, **25**, 2613–2616.
- 29 C. E. Bamberger and G. M. Begun, *J. Am. Ceram. Soc.*, 1987, **70**, C-48–C-51.
- 30 T. Kasuga, M. Hiramatsu, A. Hoson, T. Sekino and K. Niihara, *Adv. Mater.*, 1999, **11**, 1307.
- 31 Y. Su, M. L. Balmer and B. C. Bunker, *J. Phys. Chem. B*, 2000, **104**, 8160–8169.
- 32 M. Ocana, J. V. Garcia-Ramos and C. J. Serna, *J. Am. Ceram. Soc.*, 1992, **75**, 2010.
- 33 B. Mihailova, M. Gospodinov, B. Güttler, R. Stosch and U. Bismayer, *J. Phys.: Condens. Matter*, 2007, **19**, 275205.
- 34 J. Kreisel, A. M. Glazer, P. Bouvier and G. Lucazeau, *Phys. Rev. B: Condens. Matter*, 2001, **63**, 174106.
- 35 D. A. Porter and K. E. Easterling, *Phase Transformation in Metal and Alloys*, 2nd edn, CRC Press, UK, 1992.
- 36 C. N. R. Rao, *Mater. Sci. Eng., B*, 1993, **18**, 1–21.
- 37 W. D. Kingery, H. K. Bowen and D. R. Uhlmann, *Introduction to Ceramics*, John Wiley & Sons, Inc., New York, 2nd edn, 1976.
- 38 B. Noheda and D. E. Cox, *Phase Transitions*, 2006, **79**, 5–20.
- 39 D. E. Cox, B. Noheda, G. Shirane, Y. Uesu, K. Fujishiro and Y. Yamada, *Appl. Phys. Lett.*, 2001, **79**, 400–402.
- 40 J. M. Kiat, Y. Uesu, B. Dkhil, M. Matsuda, C. Malibert and G. Calvarin, *Phys. Rev. B: Condens. Matter*, 2002, **65**, 064106-4.
- 41 B. Noheda, J. A. Gonzalo, L. E. Cross, R. Guo, S.-E. Park, D. E. Cox and G. Shirane, *Phys. Rev. B: Condens. Matter*, 2000, **61**, 8687–8695.
- 42 M. Iwata, T. Araki, M. Maeda, I. Suzuki, H. Ohwa, N. Yasuda, H. Orihara and Y. Ishibashi, *Jpn. J. Appl. Phys.*, 2002, **41**, 7003–7006.
- 43 S. Andersson and A. D. Wadsley, *Acta Crystallogr.*, 1962, **15**, 194–201.
- 44 A. S. Bhalla, R. Guo and R. Roy, *Mater. Res. Innovations*, 2000, **4**, 3–26.
- 45 Z. L. Wang and Z. C. Kang, *Functional and Smart Materials*, Plenum Press, New York, 1998.
- 46 K. Tkacz-Smiech, A. Kolezynski and W. S. Ptak, *Solid State Commun.*, 2003, **127**, 557–562.
- 47 L. Klinger and E. Rabkin, *Materialwiss. Werkstofftech.*, 2005, **36**, 505–508.
- 48 W. W. Mullins, *J. Appl. Phys.*, 1957, **28**, 333–339.
- 49 J. W. Martin and R. D. Doherty, *Stability of Microstructure in Metallic Systems*, Cambridge University Press, London, 1976.
- 50 T. Motohashi and T. Kimura, *J. Am. Ceram. Soc.*, 2008, **91**, 3889–3895.
- 51 S. Karim, M. E. Toimil-Molares, A. G. Bologh, W. Ensinger, T. W. Cornelius, E. U. Khan and R. Neumann, *Nanotechnology*, 2006, **17**, 5954–5959.
- 52 D. Duft, T. Achtzehn, R. Müller, B. A. Huber and T. Leisner, *Nature*, 2003, **421**, 128.
- 53 D. J. Srolovitz and C. V. Thompson, *Thin Solid Films*, 1986, **139**, 133–141.